PNAS

Compositional and thermal state of the lower mantle from joint 3D inversion with seismic tomography and mineral elasticity

Xin Deng[a] (ID), Yinhan Xu[a], Shangqin Hao[a,b] (ID), Youyi Ruan[c,d], Yajie Zhao[a] (ID), Wenzhong Wang[a,e,f], Sidao Ni[g], and Zhongqing Wu[a,e,f,1] (ID)

The compositional and thermal state of Earth's mantle provides critical constraints on the origin, evolution, and dynamics of Earth. However, the chemical composition and thermal structure of the lower mantle are still poorly understood. Particularly, the nature and origin of the two large low-shear-velocity provinces (LLSVPs) in the lowermost mantle observed from seismological studies are still debated. In this study, we inverted for the 3D chemical composition and thermal state of the lower mantle based on seismic tomography and mineral elasticity data by employing a Markov chain Monte Carlo framework. The results show a silica-enriched lower mantle with a Mg/Si ratio less than ~1.16, lower than that of the pyrolitic upper mantle (Mg/Si = 1.3). The lateral temperature distributions can be described by a Gaussian distribution with a standard deviation (SD) of 120 to 140 K at 800 to 1,600 km and the SD increases to 250 K at 2,200 km depth. However, the lateral distribution in the lowermost mantle does not follow the Gaussian distribution. We found that the velocity heterogeneities in the upper lower mantle mainly result from thermal anomalies, while those in the lowermost mantle mainly result from compositional or phase variations. The LLSVPs have higher density at the base and lower density above the depth of ~2,700 km than the ambient mantle, respectively. The LLSVPs are found to have ~500 K higher temperature, higher Bridgmanite and iron content than the ambient mantle, supporting the hypothesis that the LLSVPs may originate from an ancient basal magma ocean formed in Earth's early history.

composition | thermal state | lower mantle | LLSVPs | MCMC

The Earth's lower mantle between the depths of 660 km and 2,891 km is of broad interest since it occupies ~55% of the volume and ~52% of the mass of the Earth. Its compositional and thermal state is key to understanding the dynamics, evolution, and chemical stratification of the Earth. For example, the compositional difference between the lower mantle and the pyrolitic upper mantle reflects the efficiency of mantle mixing (e.g., refs. 1–4). The 3D compositional structure of the lower mantle is prerequisite for identifying the local enrichment of intrinsically strong Bridgmanite (Bdg), which could prevent efficient mantle mixing, flatten rising plumes and subducting slabs, and provide a reservoir to host primordial geochemical signatures (5). The compositional and temperature features of the large low-shear-velocity provinces (LLSVPs) in the lowermost mantle beneath Africa and the Pacific (6) are also crucial for understanding their origins and the implications for Earth's evolution. Temperature influences the mantle dynamics. Higher temperature usually corresponds to lower density and viscosity. A homogeneous lateral temperature distribution means a high efficiency of the mantle convection. Thus, the lateral temperature distribution can be related to heterogeneity scales and style of mantle convection.

The composition and temperature distributions control density structure of the lower mantle. The lateral density variation can be constrained from solid Earth tide, normal modes splitting, geoid, and free-air gravity anomaly (e.g., refs. 7–12). However, the results from these studies are restricted to long-wavelength models and inconsistent with each other especially in the lowermost mantle, where the LLSVPs regions may be denser (7, 9, 10, 12) or lighter (8, 11) than the surrounding mantle. High-resolution density structure has been inferred from velocity variations based on the simple scaling relation "$d\ln\rho/d\ln V_S = 0.4$" (13). However, this relation is not reliable because composition and temperature may have different effects on the velocities and the density. For instance, higher temperature and increased iron content may both reduce the sound velocity but they have an opposite effect on the density. Fixing a constant scaling relation between density and velocity variations at all locations implicitly assumes that the origin of velocity anomalies is unique, either thermal or compositional, which is unlikely. In turn, if the 3D compositional and thermal state of the lower mantle are well known, a 3D density structure of the lower mantle can be inferred through the equation of state.

Significance

The Earth's lower mantle occupies ~55% of the volume and ~52% of the mass of the Earth. Its 3D compositional and thermal state is fundamentally important in understanding all kinds of geology processes that occur both within Earth's interior and surface, but remains unclear. In this study, the 3D chemical composition and thermal state of the lower mantle are constrained based on seismic tomography and mineral elasticity data. The resulting thermal, compositional, and density structures of the lower mantle provide important information on the dynamics, evolution, and chemical stratification of the Earth.

In spite of great importance, the knowledge on the 3D compositional and thermal state of the lower mantle remains unclear. Several studies have attempted to recover the thermochemical structure of the lower mantle from seismic tomography models. A first attempt was made by Trampert et al. (10), but with a low radial resolution. Mosca et al. (9) improved the vertical resolution with a similar approach, but these two studies considered only temperature, global iron content, and Bridgmanite/ferropericlase in their models (9, 10). Obtaining the 3D compositional and thermal structure requires both the high-resolution seismic tomography model and the high-quality elasticity data of minerals. Until now many seismic tomography models have been published to map the structure and dynamics of Earth's interior (e.g., refs. 14–17) including the model GLAD-M25 (18) based on global full waveform inversion, which dramatically increases the resolution. By developing an elastic method with a computational workload that is only one-tenth of the conventional method (19, 20), we successfully obtained the high-quality elasticity data of the lower mantle minerals at the pressure and temperature conditions of the lower mantle (21–24).

Combining the literature seismic tomography models and the reliable mineral elasticity data, the chemical composition and thermal state of the lower mantle can be constrained. Temperature and the proportions of the major minerals as well as their Fe content were treated as the model parameters to match the seismic velocity tomography at each point in the model. However, the process was not easily achieved given the large model space involved. Besides, the inversion was nonunique, a range of results may be able to provide acceptable fits to the observations and the trade-off among the parameters should be clarified. Therefore, a Bayesian inference approach was applied in the study, which involved the use of probability distributions to describe the various states of model parameters. The samples were obtained using Markov chain Monte Carlo (MCMC) simulations (*SI Appendix,* Fig. S1). In this way, we basically considered all the models that can fit to the observations and overcame the nonuniqueness of the inversion. The final results recovered the input seismic tomography models well and provided important insights on the Earth's evolution and dynamics.

Results and Discussion

1. Model Evaluation. *SI Appendix,* Fig. S2 illustrates the posterior probability distributions of the model parameters, including temperature, mineral proportions, and their Fe content, as well as the velocities and density derived from these parameters at 1,000 km depth in the inversion of model GLAD-M25 (18). The parameters are constrained well, and their bounds are reasonable in the inversion as their probabilities show near-normal distributions within the ranges specified by the upper and lower bounds in *SI Appendix,* Table S1, except for CaPv, which has a near-uniform posterior distribution, with a large standard deviation (SD). Nevertheless, CaPv only comprises approximately 7% of the peridotitic mantle, thus having minor influences on the inversion results.

SI Appendix, Figs. S3 and S4 show the distribution of all the accepted sampled models for all the model parameters at the point (21°N 152°W) and two depths in the inversion of model GLAD-M25 (18). The accepted samples cover substantial regions of the model space. Although trade-offs among model parameters exist (*SI Appendix,* Figs. S3 and S4 and Text S1), the posterior distribution of the parameters provides a good representation for the whole model space that could provide acceptable fits to the observations.

SI Appendix, Fig. S5 shows the resulting radial averages of velocities and density with respect to the reference velocity model

GLAD-M25 (18) and the density profile from PREM. The resulting profiles are almost identical to the reference models, demonstrating the validity of the inversion results. The resulting velocity structures are also compared with GLAD-M25 at different depths (*SI Appendix,* Fig. S6). The final model replicates the reference seismic tomography well, suggesting the self-consistence of the method.

2. Radial Lower Mantle Structure. The obtained lower mantle geotherm is compared with previous lower mantle temperature studies (Fig. 1*A*). Numerous adiabatic geotherms have been proposed with different gradients and potential temperatures (e.g., refs. 25–29). The previously determined adiabats show large discrepancies. The temperature profiles proposed by Anderson et al. (25) and Stacey (30) with steep temperature gradients predict much higher temperatures than that of Brown and Shankland (26) with small isentropic gradient. Although the obtained geotherm is higher than the previous adiabatic estimations, it has a temperature gradient similar to the adiabatic geotherms by Anderson et al. (25) and Stacey (30) up to the depth of ~2,700 km, suggesting an adiabatic lower mantle. Then the temperature rises with a much higher gradient and finally reaches about 3,700 K near the CMB, indicating the presence of a thermal boundary layer at the bottom of the mantle. Our temperature results overall match with the profile from Stacey (30), which indicates that the temperature increases rapidly approaching the CMB.

The temperature at the CMB (T_{CMB}) is a key parameter controlling the dynamics and thermal evolution in the mantle and the core. The lower mantle solidus from the mantle side (e.g., ref. 31) and the melting temperature of iron alloy with light element from the outer core side (e.g., ref. 32) provide constrains on T_{CMB}. The predicted T_{CMB} ranges from 3,400 K to 4,300 K, with 3,800 K to 4,200 K most plausible by determining the melting curve of the silicate mantle and from the core geotherm (31) (Fig. 1*A*). The temperature profile in our study suggests a T_{CMB} higher than 3,700 K, consistent with previous estimations (31).

The radial average mineral proportions are illustrated in Fig. 1*B*. Based on our results, Bdg occupies around 84% of the upper lower mantle (Fig. 1*D*). At around 2,500 km depth, Bdg starts to transform to PPv, and they both could exist in the lowermost mantle. Bdg content decreases to about 45% and that of PPv increases to around 32% at 2,800 km depth. Fp remains ~9% in the upper lower mantle. It decreases slightly starting from around 1,400 km depth and attains its minimum of about 7% at a depth of 1,900 km, where the spin cross-over of Fp generates the largest softening in bulk modulus (24). Then it increases significantly with depth and reaches ~16% at 2,800 km depth. No significant variation has been found in the content of CaPv. It retains ~8% throughout the entire lower mantle.

The iron in Bdg stays about 10% in the upper lower mantle and increases from 2,600 km depth to ~13% at a depth of 2,800 km (Fig. 1*C*). Controlled by the depth-dependent Fe-Mg exchange coefficient (33), the iron content of Fp fluctuates from ~16 to ~21% throughout the lower mantle and that of PPv decreases with depth from ~7 to ~3%. The iron concentrations of all the models agree well with each other.

While it is widely accepted that the upper mantle has a pyrolitic bulk composition with a Mg/Si ratio of ~1.3, large discrepancies for the Mg/Si ratio in the lower mantle exist in previous studies. A variety of chemical composition models, ranging from chondritic to pyrolitic with a Mg/Si ratio from ~1.0 to 1.3 (e.g., refs. 1–4), have been proposed for the lower mantle. If the lower mantle has a chondritic composition (e.g., refs. 1 and 2), which is different from that of the upper mantle, the mantle could be chemically and dynamically layered. If the lower mantle has a pyrolitic composition
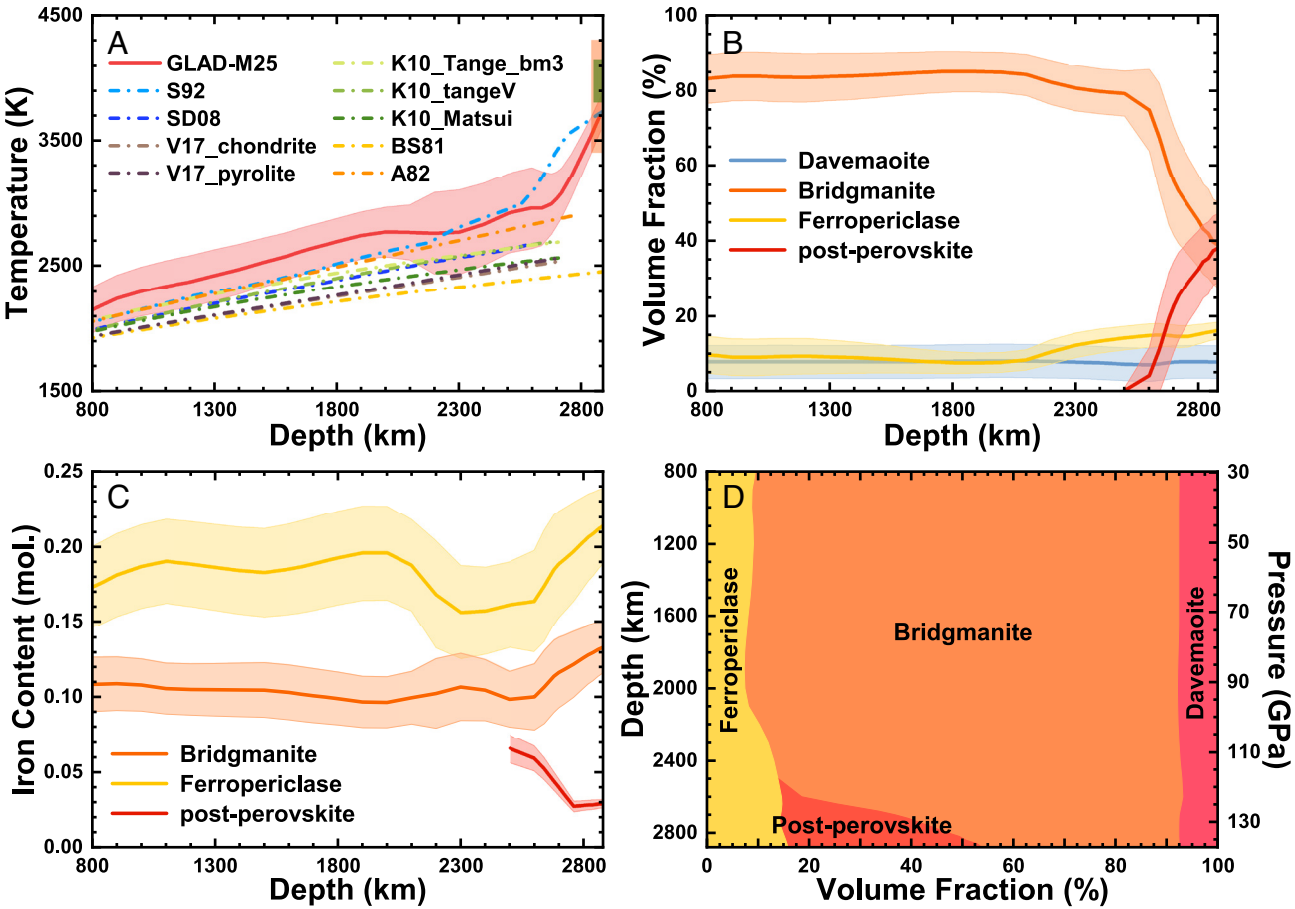
Fig. 1. (*A*) The lower mantle geotherm in the inversion of model GLAD-M25 (18) compared with previous lower mantle temperature studies (25–30). The orange shaded area indicates the predicted T_{CMB} in previous studies, and the green shaded area corresponds to the most likely temperature at the CMB (31). (*B*) The radial average volume fractions of each mineral in the inversion. (*C*) The radial average iron contents of each mineral in the inversion. (*D*) The radial average mineralogical model of the lower mantle as a function of depth (pressure).

(e.g., ref. 3), the same as the upper mantle, then the whole-mantle convection is expected. But in this case, the Mg/Si ratio would be much higher than that of the chondrites (Mg/Si = 1.05), which are usually taken to represent the Mg/Si ratio of the bulk Earth.

The average Mg/Si ratio of the entire lower mantle is estimated to be 1.04 to 1.08 in this study, if the composition of $\left(Mg_{1-x}Fe_x\right)SiO_3$ in Bdg is considered (Table 1). However, as the major host of Fe^{3+} and Al^{3+} in the lower mantle, Bdg could accommodate trivalent cations in its structure, thus affecting the Mg/Si ratio. The $Fe^{3+}/\sum Fe$ ratio of Bdg in the lower mantle could reach 0.6 and even up to 0.9 by experimental and computational studies (e.g., refs. 3 and 34). Considering the composition of

$\left(Mg_{1-x}Fe_x^{3+}\right)\left(Si_{1-x}Al_x^{3+}\right)O_3$ instead of $\left(Mg_{1-x}Fe_x\right)SiO_3$ in Bdg, which would not noticeably change the Bdg proportion and its Fe content since $\left(Mg_{1-x}Fe_x^{3+}\right)\left(Si_{1-x}Al_x^{3+}\right)O_3$ and $\left(Mg_{1-x}Fe_x\right)SiO_3$ with the same Fe content have almost identical density and elasticity (21, 23) (*SI Appendix*, Fig. S7), the upper limit of the average lower mantle Mg/Si ratio is estimated to be 1.13 to 1.19 (Table 1), implying a silica-enriched composition relative to the pyrolitic upper mantle with a Mg/Si ratio of ~1.3. Therefore, the mantle convection process may have not efficiently mixed the whole-mantle composition throughout the Earth's history to a homogeneous state (e.g., refs. 1 and 2). The whole-mantle convection models with a pyrolitic composition in the asthenosphere indeed predicted a moderate enhancement of basalt in the lower mantle with a Mg/Si ratio of ~1.15 (35), coinciding well with our study. It is also possible that the widely observed material exchange between the upper and lower mantle, like slabs penetrating into the lower mantle and plumes rising beneath hotspots, did not happen until recently in Earth's history (36) and the time is too short to completely homogenize the lower mantle. The average Mg/Si ratio of the whole mantle is ~1.2, higher than the Mg/Si ratio of the bulk Earth (Mg/Si = 1.05). Geochemical evidence suggests that the metal core of Earth might be a reservoir of silicon (e.g., ref. 37), thus the depletion of silicon in the mantle might be balanced by the presence of silicon in the core. Our results suggest that ~5 wt.% of silicon in the metal core is needed to match the Mg/Si ratio of chondrites, in agreement with previous estimates (38).

Table 1. The upper and lower limits of Mg/Si ratio for different seismic tomography models

	Lower limit	Upper limit
GLAD-M25	1.042	1.148
GLAD-M25 (Al- and Fe³⁺-bearing Bdg)		1.128
GyPSuM	1.071	1.178
HMSL	1.057	1.166
S40RTS	1.081	1.189
SP12RTS	1.077	1.184

The upper limit was calculated by replacing $(Mg_{1-x}Fe_x)SiO_3$ with $(Mg_{1-x}Fe_x^{3+})(Si_{1-x}Al_x^{3+})O_3$ in the inversion results using the elasticity of $(Mg_{1-x}Fe_x)SiO_3$. GLAD-M25 (Al- and Fe³⁺-bearing Bdg) shows the Mg/Si ratio by using the elasticity of $(Mg_{1-x}Fe_x^{3+})(Si_{1-x}Al_x^{3+})O_3$ directly in the inversion of model GLAD-M25 as reference.

3. Lateral Variation in the Lower Mantle. The lateral temperature frequency distributions at different depths are shown in Fig. 2, and the SD of the distribution is shown in Fig. 2E with depths from 800 km to 2,200 km. At depths shallower than 1,600 km (Fig. 2 A and B), the frequency distribution is well fitted with a Gaussian distribution for the case of a narrow SD of 120 to 140 K, similar to the lower mantle transition zone determined by Zhao et al. (39) based on the sensitivity of the amount of akimotoite on the temperature distribution and by Wang et al. (40) based on the temperature and water effects on the seismic tomography and topography of the 660-km discontinuity. The SD is related to heterogeneity scales and style of mantle convection. A low SD means that the temperatures are homogeneous globally, revealing a high efficiency of the mantle convection, while a high SD indicates that the temperatures are spread out over a wide range, suggesting that the mantle has not been well homogenized by the mantle convection throughout the Earth's history. As shown in Fig. 2E, the SD remains around 120 to 140 K up to ~1,600 km depth. Then the distribution gets wider and the SD increases rapidly and reaches 250 K at 2,200 km depth, suggesting that the upper lower mantle is mixed better than the lower part. The depth of ~1,600 km coincides with the upper limit of the LLSVP beneath Africa which sits on the CMB and could reach up to a height of 1,200 km (e.g., ref. 41), implying the inhomogeneity of the deep lower mantle. At depths greater than 2,200 km, the distribution cannot be fitted by the Gaussian distribution (Fig. 2D), probably because of the large lateral inhomogeneity in the lowermost mantle (6). However, we cannot rule out the possibility that it might be caused by the poor resolution due to uneven distribution of

earthquakes and seismic stations and limited ray coverage in the tomography models especially at depths greater than ~2,200 km. The temperature contrast between the coldest and the hottest regions increases from ~1,100 K to ~1,500 K between 1,000 and 2,000 km depth, and reaches ~1,600 K at 2,500 km depth, consistent with the previous studies (42, 43).

Numerous seismic velocity anomalies with velocity both higher and lower than the ambient mantle at different scales have been detected in the lower mantle with seismological studies (e.g., refs. 15 and 18). The seismic velocities are determined by the composition and temperature. The lateral temperature distribution and the iron content in the inversion of GLAD-M25 at different depths are also shown in Fig. 3. Their uncertainties are shown in *SI Appendix*, Fig. S8. As expected, the low-velocity structures in the tomography correspond to high temperatures (Figs. 3 E, J, and O and 4P) (13, 17). The iron-enriched areas also coincide well with the low-velocity structures, indicating the velocity reducing effect of iron especially in the lowermost mantle.

Although the seismic velocities of mineral assemblages are controlled by their composition and temperature, the relative importance of these two contributions at different depths remain unclear. Here, we examined the origins of the seismic velocity anomalies. The contribution of temperature variations on the seismic velocity anomalies is evaluated by calculating the velocity structures with the resulting temperature structures and the fixed average composition at each depth (ΔV_S^T) (Fig. 5 A–D). Likewise, the contribution of composition variations on the seismic velocity anomalies is also evaluated by calculating the velocity structures with the fixed average temperature at each depth (ΔV_S^C) (Fig. 5 E–H).
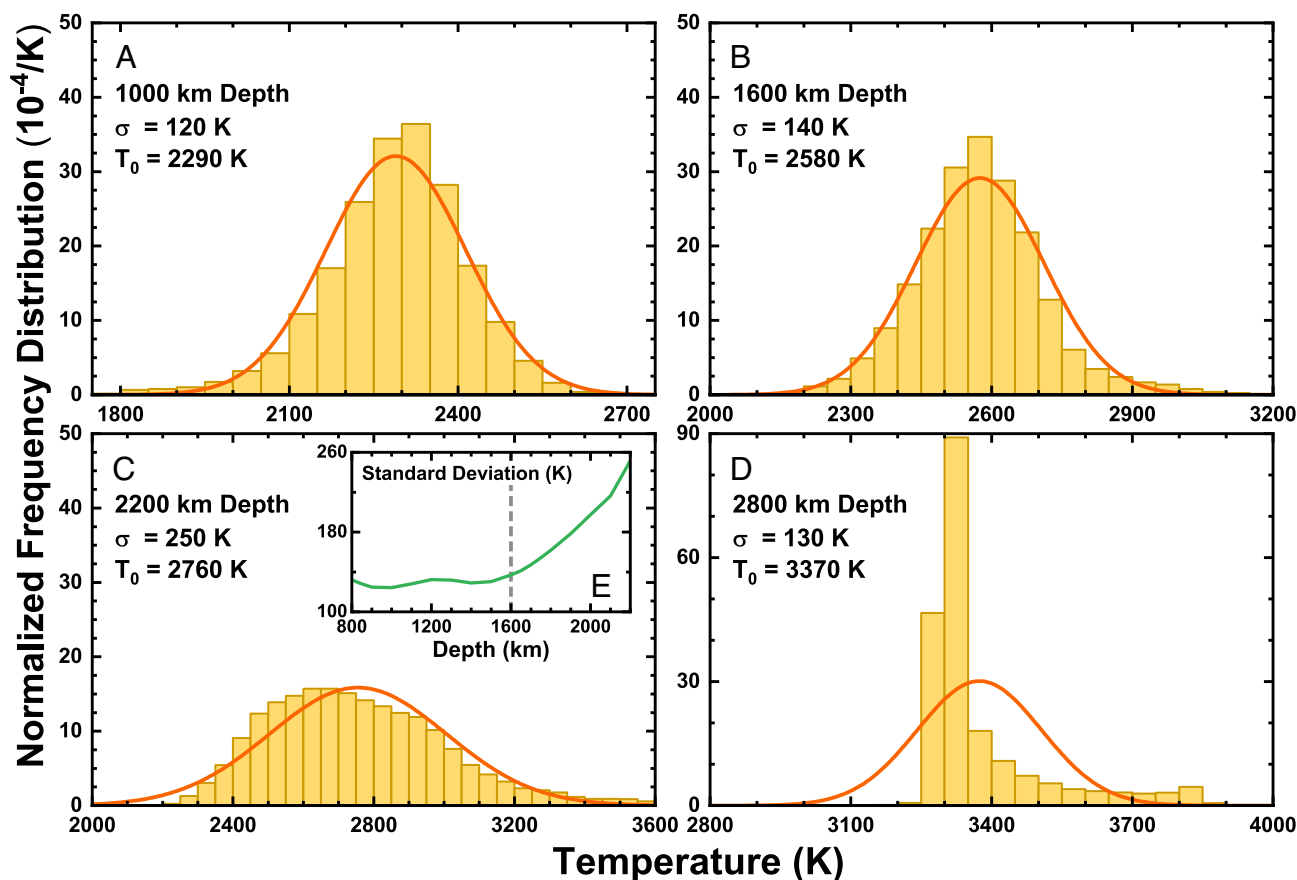
Fig. 2. (A–D) The lateral temperature frequency distributions (yellow bars) for the model GLAD-M25 (18) fitted by Gaussian distributions (orange lines) at different depths from 1,000 km to 2,800 km. σ represents the SD of the temperature distribution, T_0 corresponds to the average temperature at each depth. (E) The SD of the temperature distribution as a function of depth.
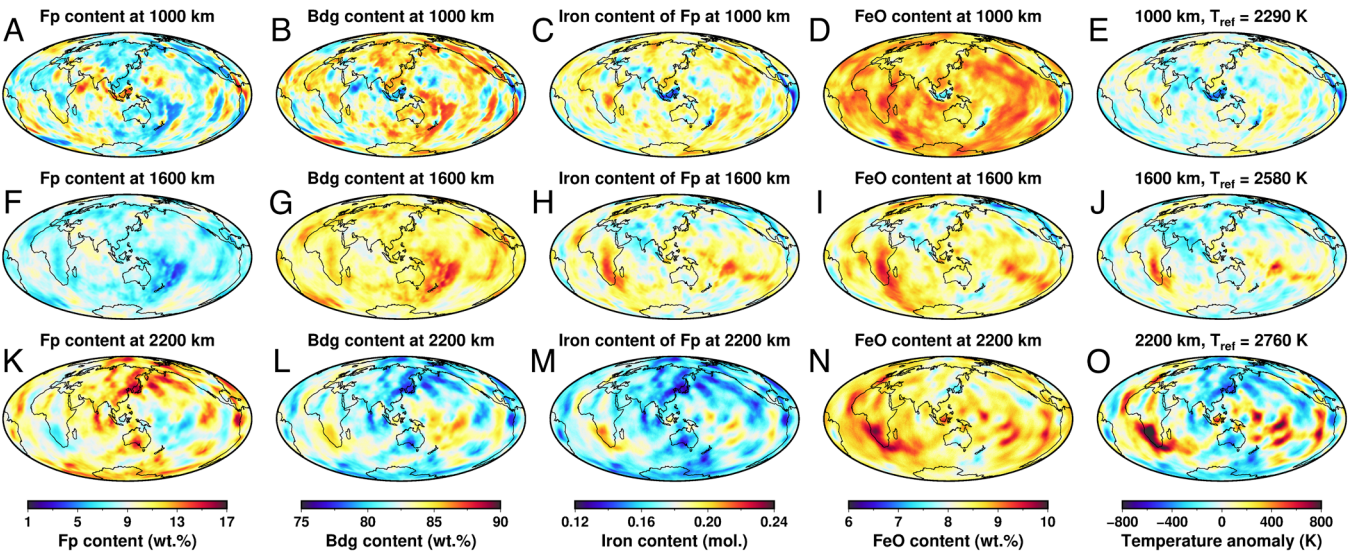
Fig. 3. The weight fraction of each mineral, the iron content of Fp, the FeO content, and the temperature distribution in the inversion of model GLAD-M25 (18) at different depths from 1,000 km to 2,200 km.

The relationships between ΔV_S^T and ΔV_S^C at each depth are shown in Fig. 5 *I–L*. Temperature has much larger effects than composition in the upper lower mantle, especially for low-velocity anomalies.

However, the composition effect dominates at deeper depths, particularly in the lowermost mantle. The velocity variations at 2,800 km depth (Fig. 5 *D*, *H*, and *L*) are almost controlled by the composition.
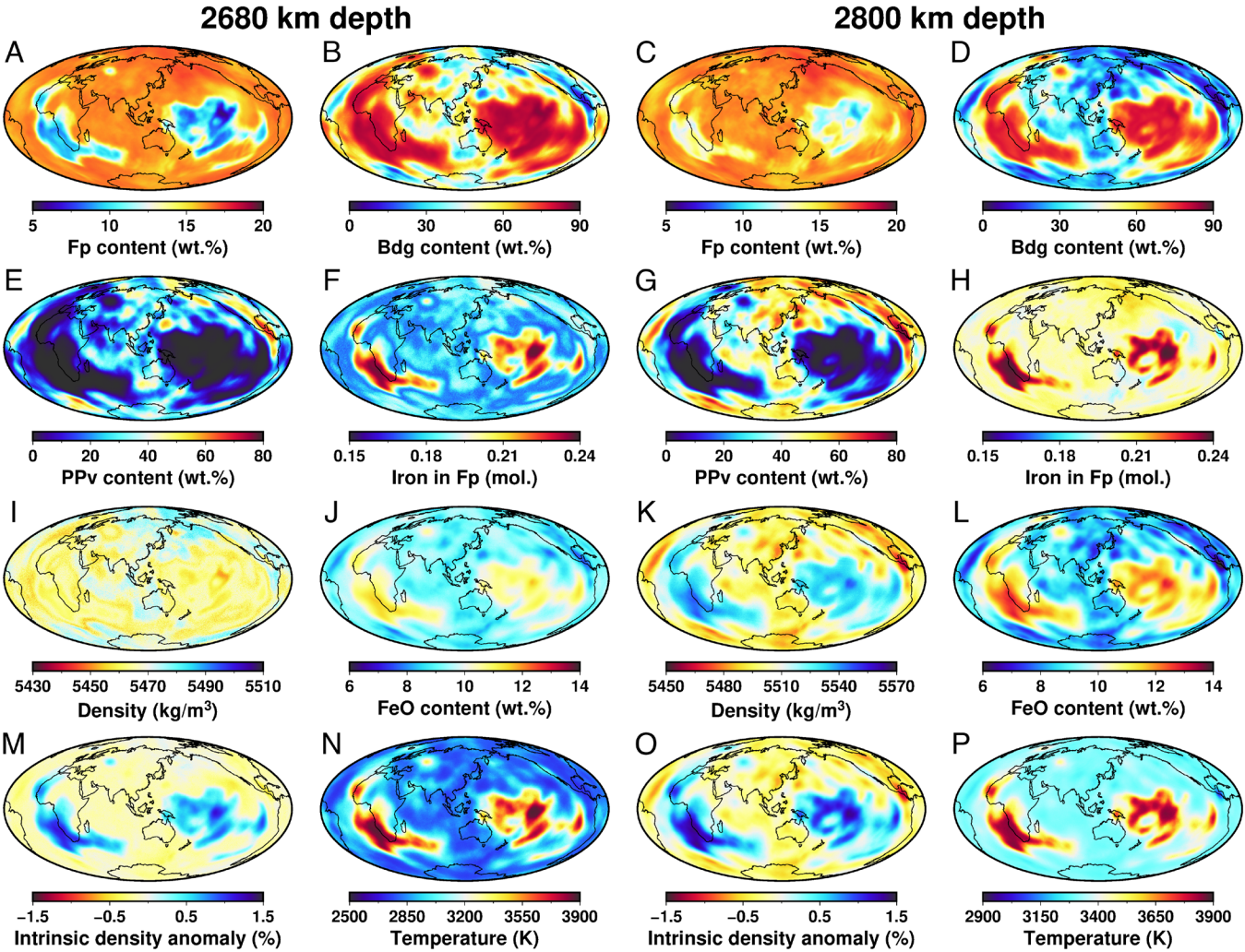
Fig. 4. The compositional and temperature distributions of the resulting model in lowermost mantle (2,680 km and 2,800 km depth) in the inversion of model GLAD-M25 (18). (*M* and *O*) The intrinsic density anomaly structure assuming the temperatures are equal to the average temperature at each depth.

V$_S$ anomaly by temperature (ΔV_S^T)   V$_S$ anomaly by composition (ΔV_S^C)
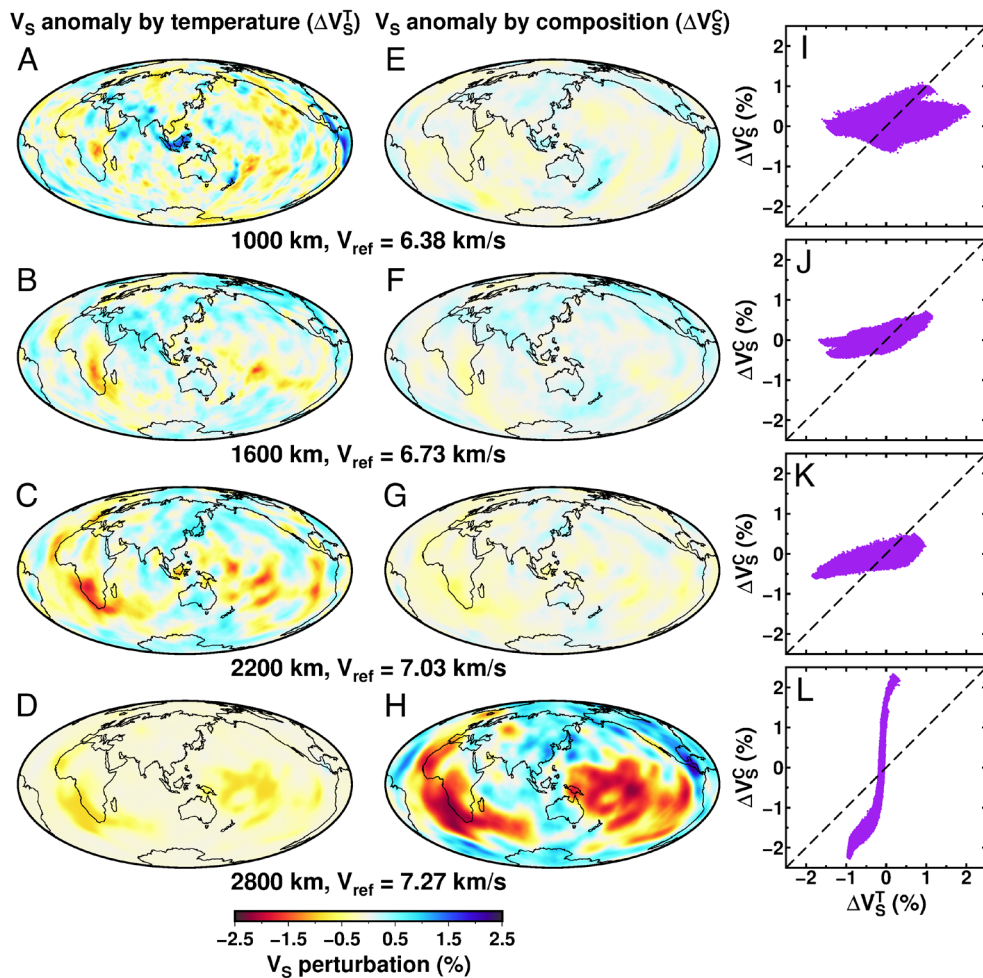
Fig. 5. The contributions of variations in temperature (ΔV_S^T) and composition (ΔV_S^C) on the V_S structure at different depths from 1,000 km to 2,800 km in the inversion of model GLAD-M25 (18). The left column (*A-D*) shows the structures of V_S by temperature (ΔV_S^T), the middle column (*E-H*) shows the V_S anomaly by composition (ΔV_S^C), and the right column (*I-L*) plots the relationships between ΔV_S^T and ΔV_S^C at each depth.

Therefore, the velocity heterogeneities in the upper lower mantle can be nearly treated as thermal anomalies, while the velocity heterogeneities in the lowermost mantle mainly result from chemical origins.

4. Compositional and Thermal Structure of the LLSVPs. LLSVPs are the two large-scale low-velocity heterogeneities in the lowermost mantle beneath Africa and the Pacific (6), which cover up to 30% of the core-mantle boundary (CMB) and could reach up to a height of 1,200 km (41). They are characterized by a reduction in both V_P and V_S by over 0.5% and 2%, but an increase in the bulk sound velocity V_Φ ranging from 0.5 to 1%. The anticorrelation between V_S and V_Φ anomalies suggests a chemical origin of the LLSVPs. Besides, the LLSVPs may be denser and hotter than the surrounding mantle (6). Their nature and origin have significant implications for the chemical and dynamical evolution of the Earth but remain debated.

Trampert et al. (10) attempted to recover the thermo-chemical structure from normal mode data, and suggested that the LLSVPs regions are enriched in iron and Bdg by ~1 to 2% and ~6 to 9%, respectively, although with nearly no temperature anomalies. Mosca et al. (9) updated their models with higher resolution and PPv considered. They confirmed such excess in iron and Bdg, with somewhat larger iron excess (~3 to 4 wt.% in FeO content). But the LLSVPs regions are 200 to 300 K colder than the surrounding mantle at 2,600 km depth in their model. Combining results from

geodynamics and mineral physics, Deschamps et al. (44) found that the LLSVPs unlikely consist of recycled oceanic crust (MORB), as it shows a high-velocity anomaly. Instead, material enriched in iron by ~3% and in (Mg, Fe)-perovskite by ~20% compared to the regular mantle with high temperatures provides a good explanation for the LLSVPs. Combining shear velocity anomalies and seismic attenuation models, Deschamps et al. (45) found that the LLSVP beneath the Pacific may be hotter by ~350 K and enriched in FeO by ~3.5 to 4.5%, supporting a thermochemical nature for LLSVPs. Using principal component analysis, Vilella et al. (46) found that the LLSVPs should be depleted in Fp and have high temperatures.

To shed more light on their structures, the temperature distribution at 2,800 km depth in the model is shown in Fig. 4*P*. The most pronounced features in the figure are the high-temperature anomalies up to 500 K beneath Africa and the Pacific, coinciding with the LLSVP regions. The chemical composition at 2,800 km depth in the model is also illustrated in Fig. 4. Their uncertainties are shown in *SI Appendix*, Fig. S9. Bdg transforms to PPv within the lowermost mantle with a phase boundary of ~5 GPa thickness and a large positive Clapeyron (*P-T*) slope (47), indicating that Bdg could retain in the lowermost mantle with high-temperature anomaly. The Bdg and PPv contents are 45% and 32% on average at 2,800 km depth, respectively. However, their spatial distributions are not uniform. Bdg is enriched in the LLSVPs regions up to an average content of 77%. Outside the LLSVPs, Bdg only

consists about 25%. On the contrary, PPv makes up around 50% outside the LLSVPs and could even reach up to 77% beneath Central America, coinciding with previous studies (48). Inside the LLSVPs, PPv is very depleted (Fig. 4G). LLSVPs have lower Fp content compared with the ambient mantle, similar to the previous study (46), but the Fp in the LLSVPs regions contains more iron. In addition, Bdg has much higher iron containing ability than PPv (33). Therefore, the LLSVP regions are much enriched in iron with ~40% higher than the surrounding mantle at 2,800 km depth (Fig. 4L). The LLSVPs are composed of distinct chemical materials especially large amount of iron from the surrounding mantle. The enrichment of iron and Bdg in the LLSVPs has also been widely suggested in previous studies (9, 10, 44–46).

Both high iron content and high temperature can reduce the velocities but they have opposite effects on the density. The density anomalies associated with the LLSVPs remain actively debated (6). Early normal mode studies suggested that the lowermost mantle beneath the Pacific Ocean and Africa is denser than the surrounding mantle (7, 10). On the contrary, a study using Stoneley modes which is most sensitive to the lowermost mantle structure proposed that the overall density of the LLSVPs is lower than average, although they cannot exclude the presence of a denser basal structure within the lowermost 100 km (11). Another study based on tidal tomography showed that the mean density of the bottom two-thirds of the LLSVPs is about 0.5% higher than the ambient mantle, although the anomaly may be concentrated toward the very base of the mantle (12). It is still unclear whether the discrepancies in previous studies are caused by the different assumptions and observations they applied or the different sensitive areas of their methods.

The density and temperature distribution of the model are shown in Figs. 4 I and K and 6. At 2,800 km depth, the LLSVP regions are denser than the ambient mantle up to 0.8%, coinciding with the higher density structure at the base of the LLSVPs predicted by Lau et al. (12). But at depths shallower than 2,700 km, the structures are lighter than the surrounding mantle, consistent with the previous Stoneley modes study (11). Therefore, the density structure reconciles the discrepancies in previous studies (7, 9–12) with the LLSVPs denser than the ambient mantle at the base, but lighter than the ambient mantle at depths shallower than

2,700 km. The low-density structure beneath Africa could reach up to a height of 1,200 km (Fig. 6A). In order to examine the contribution of the composition on the density, we calculated the intrinsic density structure due to compositional changes only (Fig. 6B). The intrinsic densities of the LLSVPs are larger than those of the surrounding mantle, suggesting that the compositions of the LLSVPs are overall denser than those of the ambient mantle. Density anomaly depends on the chemical composition and temperature. The temperature of the LLSVP regions is ~20% (~500 K) higher than the surrounding mantle (Fig. 6C). Therefore, the lower-than-average density of the LLSVPs above the depth of 2,700 km is mainly because of the high temperature in the LLSVP regions.

The low-density feature maintains up to 1,200 km height, indicating the upper boundary of the LLSVP beneath Africa. Previous geodynamic simulations show that the iron-spin transition of Fp may control the upper boundary of LLSVPs (24, 49), although the dynamic effects of iron-spin transition are debated (50). The spin cross-over occurs at depths greater than 1,700 km and makes the density extremely sensitive to temperature (51). The high-temperature anomaly in the LLSVP structure can reduce the density much larger than that at depths above 1,700 km, where no iron-spin transition occurs, and results in a lower density compared with the ambient mantle. Thus, LLSVPs could reach and maintain a high elevation to ~1,200 km above the CMB (49).

5. Origin of the LLSVPs. The origin of the LLSVPs is controversial with a few hypotheses, including the remnants of a global layer from early Earth or a growing layer from subducted materials over time (e.g., ref. 41). Due to the large discrepancies in the shear velocity of CaPv between experimental measurements (52, 53) and between experimental and theoretical studies (54), there are debates on the velocity of the recycled oceanic crust at lowermost mantle conditions. Thomson et al. (52) suggested that the recycled oceanic crust can generate the low velocity of the LLSVPs while Deschamps et al. (44), Wang et al. (55), and Zhao et al. (56) suggested that the recycled oceanic crust shows a high-velocity anomaly. Adopting the velocity data of CaPv in Thomson et al. (52), Duan et al. (57) found that the recycled oceanic crust remains a high-velocity anomaly, which indicates
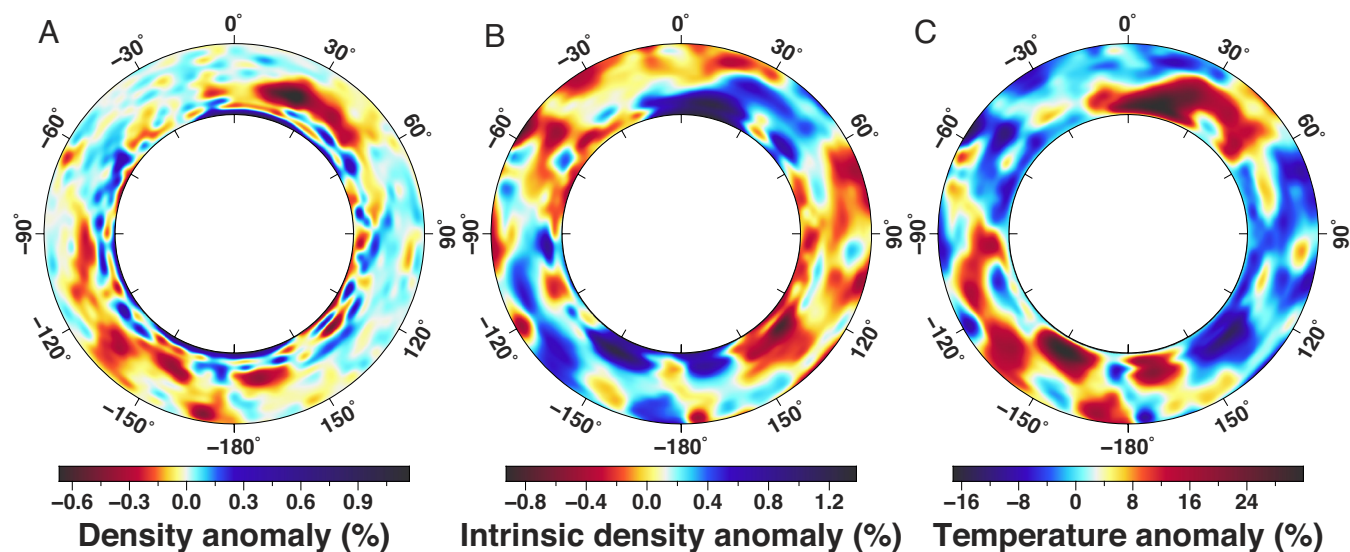
Fig. 6. The density and temperature variations in the inversion of model GLAD-M25 (18). (A) The vertical cross-sections of relative density variations (dlnρ = $\Delta\rho$ / ρ) along latitude −25°S from 800 km depth to 2,880 km depth. (B) The intrinsic density anomaly structure assuming the temperatures are equal to the average temperature at each depth. (C) The vertical cross-sections of relative temperature variations (dlnT = ΔT / T) along latitude −25°S from 800 km depth to 2,880 km depth.

that the recycled oceanic crust unlikely plays a key role in the formation of the LLSVPs.

The adiabats and density of peridotitic melt suggest that the magma ocean may crystallize from middle part (e.g., ref. 58). As a unique candidate for the hidden geochemical reservoir, the basal magma ocean also provides an attractive mechanism for the formation of LLSVPs (e.g., refs. 44 and 59). Since Fe prefers to stay in the melting phase during the crystallization of silicate melts, the basal magma ocean would be gradually enriched in iron during the solidification (59). The dense Fe-rich layer, which is heated constantly by Earth's core and retains in a high temperature, would accumulate and evolve into huge Fe-rich blocks with steep boundaries and high elevation as simulated in the geodynamic studies (e.g., refs. 49, 59, and 60). Our study shows that by the high temperature and the enrichment of iron, the aggregate of the major lower mantle minerals can exactly produce the velocity of LLSVPs, thus providing a powerful support for the basal magma ocean model from a velocity perspective.

Materials and Methods

1. Seismic Tomography Models. Although there are differences in details of various seismic tomography models, cluster analysis and spectral statistics have demonstrated coherent features of two LLSVPs in the lower mantle among different studies (61, 62). We adopt 5 recent global seismic tomography models in this study, including GyPSuM (17), HMSL (14), S40RTS (16), SP12RTS (15), and the global adjoint tomography model GLAD-M25 based on global full waveform inversion (18), with the latitude-longitude grid of 361 × 181, 90 × 45, 360 × 180, 361 × 181, 1,800 × 899, respectively. We shall note that the grid does not represent the resolution of each model, the newest model GLAD-M25 has the densest grid just because we resample it directly from the model's mesh. The GLAD-M25 model harnesses the power of waveform adjoint tomography, which resolves more details of the heterogeneities in the mantle than the ray-theory-based methods (18). Full waveform adjoint tomography, however, is a computationally very expensive method and thus far only the seismograms at period longer than 17 s have been used in the tomography. Due to the limitation of short-wavelength data in the tomography, we need to bear in mind that although GLAD-M25 might have the highest resolution in the S-wave model among the others, the P-wave model has much lower resolution than the S-wave model. Since the main conclusions of the study are not tied to a specific model, we focus on the GLAD-M25 model in the main text discussions. The results of other models are shown in supplementary material (*SI Appendix*, Figs. S10–S46 and Text S2).

2. Elasticity of Lower Mantle Minerals. The lower mantle is mainly composed of ferropericlase (Fp), Bridgmanite (Bdg), Davemaoite (CaPv), and post-perovskite (PPv). The elasticities of these minerals at lower mantle conditions are essential for constraining the composition and temperature of the deep Earth. However, experimental elasticity measurements at pressure and temperature (*P-T*) conditions corresponding to the whole-lower mantle remain difficult (63). Extrapolating the experimental data to the lower mantle conditions is inevitable, but would likely introduce large error (e.g., refs. 2 and 52). In contrast, high *P-T* can achieve in the first-principle calculations with results comparable to the experimental data. Therefore, in this study, we adopted the elastic properties of CaPv $CaSiO_3$ (54), Fp $(Mg_{1-x}Fe_x)O$ (24), Bdg $(Mg_{1-x}Fe_x)SiO_3$ (23), and PPv $(Mg_{1-x}Fe_x)SiO_3$ (22) at high *P-T* conditions by first-principle calculations.

Besides, as the major host of Fe^{3+} in the lower mantle conditions, Bdg could accommodate trivalent cations such as Fe^{3+} and Al in its structure (e.g., ref. 34). It contains 8 to 11% Fe and 7 to 11% Al if the pyrolitic composition is assumed (64). Since the elastic properties and density of Al- and Fe^{3+}-bearing $(Mg_{1-x}Fe_x^{3+})(Si_{1-x}Al_x^{3+})O_3$ are very similar to those of Fe^{2+}-bearing $(Mg_{1-x}Fe_x)SiO_3$ with the same concentration of Fe (21, 23), only the elasticity of Fe^{2+}-bearing Bdg (23) was adopted in this study, which would only introduce a small error in the determination of the Bdg proportion and its Fe content. The inversions of model GLAD-M25 with the elasticity of Al- and Fe^{3+}-bearing Bdg (21) indeed give almost the same mineral proportions and iron contents with those using the elasticity of Fe^{2+}-bearing Bdg (*SI Appendix*, Fig. S7). But the composition of $(Mg_{1-x}Fe_x^{3+})(Si_{1-x}Al_x^{3+})O_3$ is considered instead of $(Mg_{1-x}Fe_x)SiO_3$ in determining the upper limit of the Mg/Si ratio. Using the depth-dependent Fe-Mg exchange coefficient between the silicate (Bdg and PPv) and Fp (33), the Fe contents of Bdg $(Mg_{1-x}Fe_x)SiO_3$ and PPv $(Mg_{1-x}Fe_x)SiO_3$ can be obtained from the Fe concentration of Fp $(Mg_{1-x}Fe_x)O$. Therefore, only the Fe content of Fp is needed to be constrained.

3. Post-Perovskite Phase Transition. In addition, Bdg transforms to PPv at relevant *P-T* conditions corresponding to the lowermost mantle. The phase transition in the Mg end-member system ($MgSiO_3$) has a sharp phase boundary and can produce a sudden increase in the shear velocity (e.g., ref. 65). However, the incorporation of Fe and Al can broaden the transition thickness, thus smoothing the density and velocity contrast across the phase transition (e.g., refs. 47 and 64). The phase boundary in a pyrolitic mantle composition has been determined by Kuwayama et al. (47) with a ~5 GPa thickness of the Bdg + PPv two-phase region (~750 K temperature width based on the MgO pressure scale (66)). Experimental determination of the phase boundary strongly depends on the choice of the pressure scale adopted to calculate pressures (e.g., refs. 47 and 64). The Au and MgO pressure scales (66, 67) produce consistent pressure at temperatures lower than 2,000 K, however would result in different Clapeyron slopes of the phase transition, thus making large differences at higher temperature (47). If the Au pressure scale (67) is employed, PPv transforms back into Bdg above 4,800 K at the CMB pressure, much higher than the present-day estimation of CMB temperature ranging from 3,400 K to 4,300 K (31). In this case, Bdg does not appear and PPv is present ubiquitously at the CMB (47). The shear velocity of PPv is much higher than that of Bdg while the bulk sound velocity of PPv is lower than that of Bdg (21, 22). Without this phase transition, we will fail to explain the anticorrelation between the shear velocity and bulk sound velocity in the lowermost mantle (*SI Appendix*, Fig. S47). Instead, the d*P*/d*T* slope of the transition boundary is much steeper based on the MgO pressure scale (66), thus resulting in a lower transition temperature of ~3,600 K to ~4,000 K at the CMB condition. Therefore, both Bdg and PPv would exist in the lowermost mantle. Furthermore, the mutually consistent equation of states (EOSs) of MgO determined by two pressure-scale-free methods: first-principle calculations (68) and pressure-scale-free experimental measurements (69), convince us that the EOSs of MgO are reliable pressure scales (70). Therefore, in this study, we adopted the phase boundary from Kuwayama et al. (47) based on the MgO pressure scale (66). Bdg starts to transform to PPv at around 2,500 km depth under normal mantle conditions, and both of them could exist in the lowermost mantle.

4. MCMC Framework. To gain better insight into the compositional and thermal state of the lower mantle, in this study, temperature, mineral proportions of the major minerals, and the Fe content of Fp at each point in the tomography model are treated as the model parameters. Once the temperature is proposed, the other parameters can then be proposed based on the phase boundary of Bdg to PPv (47). At a certain depth and temperature, the elastic moduli and density of each composition can be obtained with the Voigt–Reuss–Hill averages:

$$\rho = \sum_i f_i \rho_i, \tag{1}$$

$$M = \frac{1}{2}\left[\sum_i f_i M_i + \left(\sum_i f_i M_i^{-1}\right)^{-1}\right], \tag{2}$$

where ρ_i, M_i, and f_i represent the density, bulk modulus (K_S) or shear modulus (G), and the volume fraction of the ith mineral, respectively. Then the compressional

and shear velocities are derived from the equations $V_P = \sqrt{\left(K_S + \frac{4}{3}G\right)/\rho}$ and $V_S = \sqrt{G/\rho}$. Thus, the model parameters can be constrained by the forward modeling of the velocity structures in the tomography. However, determining the optimal combination of these parameters is not easily achieved by such a forward modeling approach, given the large model space involved. Besides, the inversion is a nonunique process, a range of values of the parameters may be able to provide acceptable fits to the observations. To overcome these limitations, we applied a Bayesian inference approach in this study, which involves the use of probability distributions to describe the various states of model parameters.

The solution is defined as the conjunction of these probability distributions and contained in the posterior probability distributions. The samples are obtained from the posterior probability distribution by employing a MCMC scheme, which only depends on the forward modeling and associated likelihood calculations. In this way, we basically considered all the models that can fit the observations and overcame the nonuniqueness of the inversion.

The approach is formulated within a Bayesian framework, where the model parameters are delineated using probability distributions. We denote the prior probability distribution by $p(\mathbf{m})$, and the likelihood function by $f(\mathbf{d}|\mathbf{m})$. Thus, the solution can be given by the posterior probability distribution, defined as the probability of model $\mathbf{m}$, given the observations $\mathbf{d}$:

$$q(\mathbf{m}|\mathbf{d}) = p(\mathbf{m})f(\mathbf{d}|\mathbf{m}). \qquad [3]$$

Therefore, the posterior probability distribution represents how the prior knowledge of the model parameters is updated by the data. Here, we assume a uniform prior probability distribution for all the model parameters, and only their upper and lower bounds are constrained as shown in *SI Appendix*, Table S1. The likelihood function takes the form:

$$f(\mathbf{d}|\mathbf{m}) = e^{-E(\mathbf{X})}, \qquad [4]$$

and $E(\mathbf{X})$ is defined as

$$E(\mathbf{X}) = \sqrt{\left(\frac{V_P - V_P^t}{V_P^t}\right)^2 + \left(\frac{V_S - V_S^t}{V_S^t}\right)^2 + \alpha\left(\frac{\rho - \rho_{PREM}}{\rho_{PREM}}\right)^2}, \qquad [5]$$

where $\mathbf{X}$ represents a sample point of the model. V_P, V_S, and ρ are the velocities and density in $\mathbf{X}$. V_P^t, V_S^t, and ρ_{PREM} are the velocities and density from the tomography model and the PREM model, respectively. α is the weighting parameter of the density constraint (0.05 for depths shallower than 2,200 km and 0.02 for depths greater than 2,200 km). The density constraint is quite loose. However, without this constraint the resulting radial average density profile would largely deviate from the PREM model (*SI Appendix*, Fig. S48). We have also tested a range of α from 0 to 0.08 in the inversion. Different α leads to different amplitude of density perturbation, but does not change the main features of the density distribution (*SI Appendix*, Fig. S49). Since the average density can be easier matched at depths greater than 2,200 km, the density is less constrained and α is smaller at deeper depths.

To reach the limiting distribution q, a sequence of models $\mathbf{X}_i$ is generated in the Markov chain where typically each is a perturbation of the last (*SI Appendix*, Fig. S1). The initial model parameters of the chain starting point $\mathbf{X}_0$ are drawn randomly within their ranges. For each step, the current model $\mathbf{X}_{i-1}$ is perturbed randomly with the grid size shown in *SI Appendix*, Table S1 to produce a proposed new model $\mathbf{X}_i$, and $E(\mathbf{X}_i)$ can be calculated by the forward modeling approach. Then, if $E(\mathbf{X}_i)$ is smaller than $E(\mathbf{X}_{i-1})$, the new model is accepted. Otherwise, the proposed model is accepted with a probability $e^{-(E(\mathbf{X}_i)-E(\mathbf{X}_{i-1}))}$. Therefore, the acceptance criterion ratio is $\min(1, e^{-(E(\mathbf{X}_i)-E(\mathbf{X}_{i-1}))})$. Then a chain of models $\{\mathbf{X}_1, \cdots, \mathbf{X}_{N-1}, \mathbf{X}_N\}$ is generated step by step.

In this study, the first tenth of the chain is treated as the burn-in period and discarded. If the algorithm runs long enough with a wide variety of models sampled, the model generation would be stationary and the rest models in the chain $\{\mathbf{X}_{N/10+1}, \cdots, \mathbf{X}_{N-1}, \mathbf{X}_N\}$ should provide a good approximation of the posterior probability distribution for the model parameters $q(\mathbf{m}|\mathbf{d})$. Then the model outcomes are determined by evaluating the expected value of the posterior distribution, which should provide a good representation of the whole-model space that could provide acceptable fits to the observations. The evolution of the misfit function and the resulting model parameters of two grid points in GLAD-M25 are shown in *SI Appendix*, Figs. S50 and S51. The parameters have already been stabilized at the step of 2×10^6. Thus, in the application presented below, 2×10^6 iterations were applied.

Author affiliations: [a]Deep Space Exploration Laboratory / School of Earth and Space Sciences, University of Science and Technology of China, Hefei, Anhui 230026, China; [b]Institute of Geophysics and Planetary Physics, Scripps Institution of Oceanography, University of California San Diego, La Jolla, CA 92092; [c]School of Earth Sciences and Engineering, Nanjing University, Nanjing, Jiangsu 210023, China; [d]Institute of Earth Exploration and Sensing, Nanjing University, Nanjing, Jiangsu 210023, China; [e]Chinese Academy of Sciences, Center for Excellence in Comparative Planetology, University of Science and Technology of China, Hefei, Anhui 233500, China; [f]National Geophysical Observatory at Mengcheng, University of Science and Technology of China, Hefei, Anhui 233500, China; and [g]State Key Laboratory of Geodesy and Earth's Dynamics, Innovation Academy for Precision Measurement Science and Technology, Chinese Academy of Sciences, Wuhan, Hubei 430077, China

1. I. Mashino, M. Murakami, N. Miyajima, S. Petitgirard, Experimental evidence for silica-enriched Earth's lower mantle with ferrous iron dominant bridgmanite. *Proc. Natl. Acad. Sci. U.S.A.* **117**, 27899–27905 (2020).
2. M. Murakami, Y. Ohishi, N. Hirao, K. Hirose, A perovskitic lower mantle inferred from high-pressure, high-temperature sound velocity data. *Nature* **485**, 90–94 (2012).
3. X. Wang, T. Tsuchiya, A. Hase, Computational support for a pyrolitic lower mantle containing ferric iron. *Nat. Geosci.* **8**, 556–559 (2015).
4. Z. Q. Wu, Velocity structure and composition of the lower mantle with spin crossover in ferropericlase. *J. Geophys. Res. Solid Earth* **121**, 2304–2314 (2016).
5. M. D. Ballmer, C. Houser, J. W. Hernlund, R. M. Wentzcovitch, K. Hirose, Persistence of strong silica-enriched domains in the Earth's lower mantle. *Nat. Geosci.* **10**, 236–240 (2017).
6. A. K. McNamara, A review of large low shear velocity provinces and ultra low velocity zones. *Tectonophysics* **760**, 199–220 (2019), 10.1016/j.tecto.2018.04.015.
7. M. Ishii, J. Tromp, Normal-mode and free-Air gravity constraints on lateral variations in velocity and density of Earth's mantle. *Science* **285**, 1231–1236 (1999).
8. B. H. Hager, R. W. Clayton, M. A. Richards, R. P. Comer, A. M. Dziewonski, Lower mantle heterogeneity, dynamic topography and the geoid. *Nature* **313**, 541–546 (1985).
9. I. Mosca, L. Cobden, A. Deuss, J. Ritsema, J. Trampert, Seismic and mineralogical structures of the lower mantle from probabilistic tomography. *J. Geophys. Res. Solid Earth* **117**, B06304 (2012).
10. J. Trampert, F. Deschamps, J. Resovsky, D. Yuen, Probabilistic tomography maps chemical heterogeneities throughout the lower mantle. *Science* **306**, 853–856 (2004).
11. P. Koelemeijer, A. Deuss, J. Ritsema, Density structure of Earth's lowermost mantle from Stoneley mode splitting observations. *Nat. Commun.* **8**, 15241 (2017).
12. H. C. P. Lau *et al.*, Tidal tomography constrains Earth's deep-mantle buoyancy. *Nature* **551**, 321–326 (2017).
13. J. H. Woodhouse, A. M. Dziewonski, Mapping the upper mantle: Three-dimensional modeling of earth structure by inversion of seismic waveforms. *J. Geophys. Res. Solid Earth* **89**, 5953–5986 (1984).
14. C. Houser, G. Masters, P. Shearer, G. Laske, Shear and compressional velocity models of the mantle from cluster analysis of long-period waveforms. *Geophys. J. Int.* **174**, 195–212 (2008).
15. P. Koelemeijer, J. Ritsema, A. Deuss, H. J. van Heijst, SP12RTS: A degree-12 model of shear- and compressional-wave velocity for Earth's mantle. *Geophys. J. Int.* **204**, 1024–1039 (2015).
16. J. Ritsema, A. Deuss, H. J. van Heijst, J. H. Woodhouse, S40RTS: A degree-40 shear-velocity model for the mantle from new Rayleigh wave dispersion, teleseismic traveltime and normal-mode splitting function measurements. *Geophys. J. Int.* **184**, 1223–1236 (2011).
17. N. A. Simmons, A. M. Forte, L. Boschi, S. P. Grand, GyPSuM: A joint tomographic model of mantle density and seismic wave speeds. *J. Geophys. Res.* **115**, B12310 (2010).
18. W. Lei *et al.*, Global adjoint tomography–Model GLAD-M25. *Geophys. J. Int.* **223**, 1–21 (2020).
19. C. Luo *et al.*, cij: A Python code for quasiharmonic thermoelasticity. *Comput. Phys. Commun.* **267**, 108067 (2021).
20. Z. Q. Wu, R. M. Wentzcovitch, Quasiharmonic thermal elasticity of crystals: An analytical approach. *Phys. Rev. B* **83**, 184115 (2011).
21. G. Shukla, M. Cococcioni, R. M. Wentzcovitch, Thermoelasticity of Fe3+- and Al-bearing bridgmanite: Effects of iron spin crossover *Geophys. Res. Lett.* **43**, 5661–5670 (2016).
22. G. Shukla, K. Sarkar, R. M. Wentzcovitch, Thermoelasticity of iron- and aluminum-bearing MgSiO3 postperovskite. *J. Geophys. Res. Solid Earth* **124**, 2417–2427 (2019).
23. G. Shukla *et al.*, Thermoelasticity of Fe2+-bearing bridgmanite. *Geophys. Res. Lett.* **42**, 1741–1749 (2015).
24. Z. Wu, J. F. Justo, R. M. Wentzcovitch, Elastic anomalies in a spin-crossover system: Ferropericlase at lower mantle conditions. *Phys. Rev. Lett.* **110**, 228501 (2013).
25. O. L. Anderson, S. K. Runcorn, K. M. Creer, J. A. Jacobs, The Earth's core and the phase diagram of iron. *Philos. Trans. R. Soc. Lond. A* **306**, 21–35 (1982).
26. J. M. Brown, T. J. Shankland, Thermodynamic parameters in the earth as determined from seismic profiles. *Geophys. J. R. Astron. Soc.* **66**, 579–596 (1981).
27. T. Katsura, A. Yoneda, D. Yamazaki, T. Yoshino, E. Ito, Adiabatic temperature profile in the mantle. *Phys. Earth Planet. Inter.* **183**, 212–218 (2010).

28. F. D. Stacey, P. M. Davis, *Physics of the Earth* (Cambridge University Press, Cambridge, ed. 4, 2008), 10.1017/cbo9780511812910.

29. J. J. Valencia-Cardona et al., Influence of the iron spin crossover in ferropericlase on the lower mantle geotherm. *Geophys. Res. Lett.* **44**, 4863–4871 (2017).

30. F. D. Stacey, *Physics of the Earth* (Brookfield Press, Brisbane, 1992).

31. D. Andrault, J. Monteux, M. Le Bars, H. Samuel, The deep Earth may not be cooling down. *Earth Planet. Sci. Lett.* **443**, 195–203 (2016).

32. M. Hou et al., Melting of Iron Explored by Electrical Resistance Jump up to 135 GPa. *Geophys. Res. Lett.* **48**, e2021GL095739 (2021).

33. H. Piet et al., Spin and valence dependence of iron partitioning in Earth's deep mantle. *Proc. Natl. Acad. Sci. U.S.A.* **113**, 11127–11130 (2016).

34. R. Huang et al., The composition and redox state of bridgmanite in the lower mantle as a function of oxygen fugacity. *Geochim. Cosmochim. Acta* **303**, 110–136 (2021).

35. J. Yan, M. D. Ballmer, P. J. Tackley, The evolution and distribution of recycled oceanic crust in the Earth's mantle: Insight from geodynamic models. *Earth Planet. Sci. Lett.* **537**, 116171 (2020).

36. J. Korenaga, Initiation and evolution of plate tectonics on earth: Theories and observations. *Annu. Rev. Earth Planet. Sci.* **41**, 117–151 (2013).

37. R. B. Georg, A. N. Halliday, E. A. Schauble, B. C. Reynolds, Silicon in the Earth's core. *Nature* **447**, 1102–1106 (2007).

38. J. Wade, B. J. Wood, Core formation and the oxidation state of the Earth. *Earth Planet. Sci. Lett.* **236**, 78–95 (2005).

39. Y. Zhao et al., Elastic properties of Fe-bearing Akimotoite at mantle conditions: Implications for composition and temperature in lower mantle transition zone. *Fundam. Res.* **2**, 570–577 (2022).

40. W. Z. Wang, H. Zhang, J. P. Brodholt, Z. Q. Wu, Elasticity of hydrous ringwoodite at mantle conditions: Implication for water distribution in the lowermost mantle transition zone. *Earth Planet. Sci. Lett.* **554**, 116626 (2021).

41. E. J. Garnero, A. K. McNamara, S. H. Shim, Continent-sized anomalous zones with low seismic velocity at the base of Earth's mantle. *Nat. Geosci.* **9**, 481–489 (2016).

42. A. R. Oganov, J. P. Brodholt, G. D. Price, The elastic constants of MgSiO3 perovskite at pressures and temperatures of the Earth's mantle. *Nature* **411**, 934–937 (2001).

43. J. W. Hernlund, C. Thomas, P. J. Tackley, A doubling of the post-perovskite phase boundary and structure of the Earth's lowermost mantle. *Nature* **434**, 882–886 (2005).

44. F. Deschamps, L. Cobden, P. J. Tackley, The primitive nature of large low shear-wave velocity provinces. *Earth Planet. Sci. Lett.* **349**, 198–208 (2012).

45. F. Deschamps, K. Konishi, N. Fuji, L. Cobden, Radial thermo-chemical structure beneath Western and Northern Pacific from seismic waveform inversion. *Earth Planet. Sci. Lett.* **520**, 153–163 (2019).

46. K. Vilella et al., Constraints on the composition and temperature of LLSVPs from seismic properties of lower mantle minerals. *Earth Planet. Sci. Lett.* **554**, 116685 (2021).

47. Y. Kuwayama et al., Post-perovskite phase transition in the pyrolitic lowermost mantle: Implications for ubiquitous occurrence of post-perovskite above CMB. *Geophys. Res. Lett.* **49**, e2021GL096219 (2022).

48. R. D. van der Hilst et al., Seismostratigraphy and thermal structure of Earth's core-mantle boundary region. *Science* **315**, 1813–1817 (2007).

49. C. Huang, W. Leng, Z. Q. Wu, Iron-spin transition controls structure and stability of LLSVPs in the lower mantle. *Earth Planet. Sci. Lett.* **423**, 173–181 (2015).

50. Y. Li, K. Vilella, F. Deschamps, L. Zhao, P. J. Tackley, EFfects of iron spin transition on the structure and stability of large primordial reservoirs in Earth's lower mantle. *Geophys. Res. Lett.* **45**, 5918–5928 (2018).

51. Z. Wu, J. F. Justo, C. R. S. da Silva, S. de Gironcoli, R. M. Wentzcovitch, Anomalous thermodynamic properties in ferropericlase throughout its spin crossover. *Phys. Rev. B* **80**, 014409 (2009).

52. A. R. Thomson et al., Seismic velocities of CaSiO3 perovskite can explain LLSVPs in Earth's lower mantle. *Nature* **572**, 643–647 (2019).

53. S. Greaux et al., Sound velocity of CaSiO3 perovskite suggests the presence of basaltic crust in the Earth's lower mantle. *Nature* **565**, 218–221 (2019).

54. K. Kawai, T. Tsuchiya, Small shear modulus of cubic CaSiO3 perovskite. *Geophys. Res. Lett.* **42**, 2718–2726 (2015).

55. W. Wang et al., Velocity and density characteristics of subducted oceanic crust and the origin of lower-mantle heterogeneities. *Nat. Commun.* **11**, 64 (2020).

56. M. Q. Zhao et al., Thermoelastic properties of aluminous phases in MORB from first-principle calculation: Implications for Earth's lower mantle. *J. Geophys. Res. Solid Earth* **123**, 10583–10596 (2018).

57. L. Y. Duan, "Mineral properties and geoscientific implications of the subducted crust," doctoral dissertation (2022). https://dx.doi.org/10.27517/d.cnki.gzkju.2022.001831.

58. L. Stixrude, N. de Koker, N. Sun, M. Mookherjee, B. B. Karki, Thermodynamics of silicate liquids in the deep Earth. *Earth Planet. Sci. Lett.* **278**, 226–232 (2009).

59. S. Labrosse, J. W. Hernlund, N. Coltice, A crystallizing dense magma ocean at the base of the Earth's mantle. *Nature* **450**, 866–869 (2007).

60. W. Wang et al., Formation of large low shear velocity provinces through the decomposition of oxidized mantle. *Nat. Commun.* **12**, 1911 (2021).

61. V. Lekic, S. Cottaar, A. Dziewonski, B. Romanowicz, Cluster analysis of global lower mantle tomography: A new class of structure and implications for chemical heterogeneity. *Earth Planet. Sci. Lett.* **357**, 68–77 (2012).

62. J. Ritsema, V. Lekic, Heterogeneity of seismic wave velocity in Earth's mantle. *Annu. Rev. Earth Planet. Sci.* **48**, 377–401 (2020).

63. H. Marquardt, A. R. Thomson, Experimental elasticity of Earth's deep mantle. *Nat. Rev. Earth Environ.* **1**, 455–469 (2020).

64. N. Sun et al., Phase transition and thermal equations of state of (Fe, Al)-bridgmanite and post-perovskite: Implication for the chemical heterogeneity at the lowermost mantle. *Earth Planet. Sci. Lett.* **490**, 161–169 (2018).

65. K. Hirose, Postperovskite phase transition and its geophysical implications. *Rev. Geophys.* **44**, RG3001 (2006).

66. S. Speziale, C. S. Zha, T. S. Duffy, R. J. Hemley, H. K. Mao, Quasi-hydrostatic compression of magnesium oxide to 52 GPa: Implications for the pressure-volume-temperature equation of state. *J. Geophys. Res. Solid Earth* **106**, 515–528 (2001).

67. Y. Fei et al., Toward an internally consistent pressure scale. *Proc. Natl. Acad. Sci. U.S.A.* **104**, 9182–9186 (2007).

68. Z. Q. Wu et al., Pressure-volume-temperature relations in MgO: An ultrahigh pressure-temperature scale for planetary sciences applications. *J. Geophys. Res. Solid Earth* **113**, B06204 (2008).

69. Y. Kono, T. Irifune, Y. Higo, T. Inoue, A. Barnhoorn, P-V-T relation of MgO derived by simultaneous elastic wave velocity and in situ X-ray measurements: A new pressure scale for the mantle transition region. *Phys. Earth Planet. Inter.* **183**, 196–211 (2010).

70. Z. Wu, F. Lin, Evaluation of Pt and Au pressure scales based on MgO absolute pressure scale. *Sci. China Earth Sci.* **60**, 114–123 (2016).

71. X. Deng et al., Unified Structures of Temperature and Composition of Lower Mantle (USTCLM). Zenodo. https://doi.org/10.5281/zenodo.8003898. Deposited 5 June 2023.